Precipitation of Relativistic Electrons Under Resonant Interaction with Electromagnetic Ion-Cyclotron Wave Packets

V. S. Grach[1] **and A. G. Demekhov**[2,1]

[1]Institute of Applied Physics, Russian Academy of Sciences
[2]Polar Geophysical Institute
[1]46, Ul'yanov st., 603950, Nizhny Novgorod, Russia
[2]26a, Academgorodok st., 184209, Apatity, Russia

Key Points:

- Nonlinear resonant interaction with EMIC waves can either increase or decrease electron pitch angle
- For some energies pitch angle distribution stays isotropic, precipitation fluxes at strong diffusion limit
- For higher energies precipitation fluxes correspond to weak diffusion and agree with quasi-linear theory

Corresponding author: V.S. Grach, `vsgrach@ipfran.ru`

Abstract

We use numerical simulations to study the resonant interaction of relativistic electrons with rising-frequency EMIC wave packets in the H^+ band. We find that precipitation fluxes are formed by quasi-linear interaction and several nonlinear interaction regimes having opposite effects. In particular, the influence of Lorentz force on the particle phase (force bunching) decreases precipitation for particles with low equatorial pitch angles (up to 15–25°), and can even block it completely. Four other nonlinear regimes are possible: nonlinear shift of the resonance point (can cause pitch angle drift in both directions); phase bunching (slightly increases pitch angle for untrapped particles); directed scattering (strongly decreases pitch angle for untrapped particles) and particle trapping by the wave field (decreases pitch angle). Equatorial pitch angle distribution evolution during several passes of particles through the wave packet is studied. The precipitation fluxes are evaluated and compared with theoretical estimates. We show that strong diffusion limit is maintained for a certain range of energies by a wave packet with realistic amplitude and frequency drift. In this case, the quasi-linear theory strongly underestimates the precipitated flux. With increasing energy, the precipitated fluxes decrease and become close to the quasi-linear estimates.

1 Introduction

The loss of relativistic radiation belt electrons has been observed and studied theoretically for a number of years (Thorne & Kennel, 1971; Millan & Thorne, 2007; Morley et al., 2010; Engebretson et al., 2015). The resonant interaction of relativistic electrons with electromagnetic ion-cyclotron (EMIC) waves is believed to be one of the main causes of this precipitation.

Initially, resonant interaction of relativistic electrons with EMIC waves has been analyzed within the framework of the quasi-linear theory (Summers & Thorne, 2003; Jordanova et al., 2008; Shprits et al., 2009). However, along with the noise bursts of EMIC waves, quasi-monochromatic wave packets (pearls or hydromagnetic chorus emissions) with frequencies of several Hz are often observed and their amplitudes, even moderate ones, can be high enough to ensure strongly nonlinear interaction (Kangas et al., 1998; Demekhov, 2007; Engebretson et al., 2007; Engebretson et al., 2008; Pickett et al., 2010). Pearl emissions (periodic sequences of quasi-monochromatic wave packets with periods about 100 s and increasing frequency inside each packet) are explained by a passive mode locking regime of the ion cyclotron instability (Belyayev et al., 1984; Belyaev et al., 1987; Demekhov, 2007; Trakhtengerts & Rycroft, 2008). Hydromagnetic chorus emissions or EMIC triggered emissions (Pickett et al., 2010) are similar in structure to whistler mode (ELF/VLF) chorus emissions (e.g. (Santolik et al., 2003)), and they are probably generated by a similar mechanism (Trakhtengerts, 1995). Nonlinear models of hydromagnetic chorus emissions were developed by Trakhtengerts and Demekhov (2007); Omura et al. (2010); Shoji et al. (2011). It is also worth noting that the observed loss of the outer radiation belt (Morley et al., 2010) can be too fast to be explained by quasi-linear diffusion rates.

Albert and Bortnik (2009) analyzed nonlinear interaction of relativistic electrons with an EMIC wave with a constant frequency. They showed the possible role of two nonlinear regimes: phase bunching without trapping, which leads to rapid pitch angle increase and thus can decrease the precipitation flux, and particles trapping by the wave field, which results in decreasing pitch angle. Artemyev et al. (2015) showed that trapping by the EMIC wave is stable with respect to non-resonant magnetic field fluctuations.

Nonlinear interaction of relativistic electrons with a model EMIC wave packet, corresponding to the emission with rising frequency, has been studied through theoretical analysis and test particle simulations in (Omura & Zhao, 2012, 2013; Kubota & Omura,

2017; Grach & Demekhov, 2018a, 2018b). Kubota and Omura (2017) showed that combined scattering process of the nonlinear wave trapping and another nonlinear regime 'SLPA' (Scattering at Low Pitch Angle) can lead to the rapid loss of relativistic electrons. The authors explained 'SLPA'-regime by the influence of Lorentz force on the particle phase (hereafter termed force bunching).

In (Grach & Demekhov, 2018a, 2018b) it was shown that a strong non-diffusive decrease of the pitch angle of untrapped electrons can also occur for fairly high pitch angles. This effect, called directed scattering, is not related to the force bunching and occurs for a small group of particles that spend a long time near the separatrix on the phase plane far from the saddle point, i.e., in the region where the phase is opposite to the phase-bunched particles.

Long time evolution of particle distribution function as a result of nonlinear resonant interaction with a monochromatic wave (various modes) was studied by Artemyev et al. (2017, 2018). The generalized Fokker-Planck equation, allowing for nonlinear regimes, was obtained; its analytical solutions have been validated by results of test particle numerical simulations. Two nonlinear regimes were taken into account: phase bunching (nonlinear scattering) and wave trapping; those regimes cause particles fast transport in phase space in the opposite directions. As a result, the Gaussian-shaped particle distribution function was shown to reach almost isotropic stationary solution. Kubota and Omura (2017) analyzed long time evolution of particle distribution in equatorial pitch angles under the resonant interaction and found echoes of electron depletion by the localized EMIC wave packets with rising frequency. They excluded particles with initial equatorial pitch angles near the loss cone from the consideration to avoid quasi-linear effects.

In this paper, we study the evolution of pitch angle distribution function during several passes of particles through the EMIC wave packet with rising frequency. We take into account particles with low initial equatorial pitch angles (close to the loss cone) and show that such particles play an important and peculiar role in the formation of precipitated flux. We also calculate precipitated fluxes, and compare them with theoretical estimates obtained from quasi-linear equations, and analyze the roles of quasi-linear interaction and several nonlinear regimes in the flux formation.

We show that under sufficiently high but realistic wave amplitude and relatively low refractive index the influence of Lorentz force on the particle phase (force bunching) can be very significant for the particles close to the loss cone. For these particles, force bunching can increase pitch angles and even block the precipitation completely from a noticeable range of low pitch angles. We show that, in the dominant part of the considered parameter region, the pitch angle distribution in the vicinity of the loss cone is close to isotropic. The precipitation fluxes are formed as a result of several interaction regimes with opposite effects. The numerical fluxes are close to quasi-linear theoretical estimates when these estimates are applicable, and may significantly exceed them in other cases.

In section 2 we describe the simulation model. In section 3.1, we summarize known results about the possible interaction regimes and apply them to the chosen parameters, and also consider some new aspects of the force bunching. In section 3.2, we discuss the role of various interaction regimes in forming the precipitation flux. In section 4, we discuss the evolution of the pitch-angle distribution, obtain precipitation fluxes and compare the results with theoretical estimates. Section 5 is devoted to discussion and conclusions.

2 Simulation Model

2.1 Theory

For parallel-propagating EMIC waves, the resonant interaction with electrons is possible only at the anomalous cyclotron resonance, and the resonance condition is written as follows:

$$\Delta = \omega - kv_{||} + \Omega_c/\gamma = 0, \tag{1}$$

where ω and k are wave frequency and number, respectively, $v_{||}$ is field-aligned velocity, $\Omega_c = eB_0/mc$, B_0 is geomagnetic field, $e > 0$ is elementary charge, $\gamma = \sqrt{1 + [p/(mc)]^2}$, m and p are the electron rest mass and momentum, respectively.

If the external field inhomogeneity is smooth, wave magnetic field amplitude $\mathbf{B}_w$ is not too high ($B_w \ll B_0$) and wave characteristics vary slowly in time and space on the scales of $2\pi/\Omega_c$ and $2\pi/k$, respectively, the resonant interaction of a test electron with EMIC wave can be described by the following equations:

$$\frac{dW}{dt} = -ev_\perp |E_w| \sin\Psi; \tag{2}$$

$$\frac{dI_\perp}{dt} = -\frac{2e}{mB_0} p_\perp (1 - n_{||}\beta_{||}) |E_w| \sin\Psi; \tag{3}$$

$$\frac{d\Psi}{dt} = -\Delta - \frac{e}{p_\perp}(1 - n_{||}\beta_{||}) |E_w| \cos\Psi; \tag{4}$$

$$\frac{dz}{dt} = \frac{p_{||}}{m\gamma}. \tag{5}$$

Here the subscripts $\perp$ and $||$ denote projections to the transverse and parallel directions with respect to $\mathbf{B}_0$, respectively, E_w is wave electric field amplitude, $n_{||} = kc/\omega$, Ψ is the gyrophase defined as the angle between $\mathbf{p}_\perp$ and $-\mathbf{B}_w$, $\beta_{||} = v_{||}/c$, $W = (\gamma - 1)mc^2$ and $I_\perp = p_\perp^2/(mB_0)$ are the electron kinetic energy and the first adiabatic invariant respectively, and z is coordinate along the geomagnetic field. In the right-hand side of equation (4) the first term represents inertial, or kinematic bunching, while the second one represents the influence of Lorentz force on the particle phase (force bunching).

For EMIC waves, $\omega \ll \Omega_c$; thus, the resonant interaction is possible only for $k_\parallel v_\parallel > 0$ and the change in electron energy W will be insignificant: $\gamma \approx$ const (Bespalov & Trakhtengerts, 1986; Albert & Bortnik, 2009). The interaction result is described by the change in the adiabatic invariant $I_\perp$ or equatorial pitch angle Θ_L, $\mu = \sin^2\Theta_L = (p_\perp^2/p^2)(B_L/B_0)$.

Particle behavior (interaction regime) is determined by the inhomogeneity parameter $\mathcal{R} = \sigma_R R$ (Karpman et al., 1974; Albert, 1993, 2000; Albert & Bortnik, 2009; Kubota & Omura, 2017; Grach & Demekhov, 2018a), where $\sigma_R = \pm 1$ determines the effective inhomogeneity sign, and

$$R = \frac{|d\Delta/dt|}{\Omega_{tr}^2}. \tag{6}$$

Here Ω_{tr}^2 is frequency of electron oscillations in the wave field near the effective potential minimum (Grach & Demekhov, 2018a; Demekhov et al., 2006). Under real conditions, the parameter R changes both in time and in space; these changes are associated both with medium inhomogeneity (including changes in the wave packet frequency and amplitude) and nonlinear changes in the particle parameters during the interaction. However, the main features of the particle motion can be categorized based on the R values calculated at the resonance point in the linear approximation. For $R > 1$, the trajectories of all particles are infinite (all particles are untrapped), and for $R < 1$ there is a minimum of the wave effective potential, i.e. particle trapping by the wave field is possible. The trajectories of the trapped particles are finite. For resonant interaction of electrons with EMIC wave packet, which is generated near the equator and propagates away

from it, the effective inhomogeneity is negative. All the expressions below assume $\sigma_R = -1$.

The case of $R \gg 1$ corresponds to the quasi-linear regime. In this case the change in particle equatorial pitch angle (and energy) is determined by the resonance phase (Albert, 2000; Albert & Bortnik, 2009; Grach & Demekhov, 2018a):

$$\Delta\mu = K_\mu \sin(\Psi_{\rm res} - \pi/4). \tag{7}$$

Here $\mu = \sin^2\Theta_L$,

$$K_\mu = \frac{2e}{mB_0}|p_\perp(1 - n_{||}\beta_{||})E_{\rm w}|\sqrt{\frac{2\pi}{|\Psi_t^{''}|_{\rm res}}}, \tag{8}$$

$|\Psi_t^{''}|_{\rm res}$ is the absolute value of second phase time derivative at the resonance point on the unperturbed trajectory. In the quasi-linear regime, the resonance phase $\Psi_{\rm res}$ linearly depends on the initial phase Ψ_0, and for ensemble of particles equatorial pitch angle diffusion takes place:

$$\langle\Delta\mu\rangle^{\rm lin} = 0; \tag{9}$$

$$\langle\Delta\mu\rangle^{\rm lin}_{\rm rms} = \sqrt{\langle(\Delta\mu^{\rm lin} - \langle\Delta\mu\rangle^{\rm lin})^2\rangle} = K_\mu/\sqrt{2}. \tag{10}$$

Hereafter, angle brackets denote phase averaging.

For $R \le 1$, the resonant interaction is nonlinear, which leads to a drift in pitch angles for both trapped and untrapped particles. The drift direction is determined by the interaction regime and the sign of effective inhomogeneity. For $\sigma_R = -1$, phase bunching of untrapped particles increases the pitch angle by a value that depends only weakly on the initial phase (Albert, 1993, 2000; Albert & Bortnik, 2009; Grach & Demekhov, 2018a, 2018b). In some papers (Artemyev et al., 2017, 2018) this regime is called nonlinear scattering. Directed scattering (Grach & Demekhov, 2018a, 2018b) can significantly decrease equatorial pitch angle for a small group of untrapped particles. This group crosses the separatrix on the phase plane far from the saddle point (near the reflection point), i.e., in the region where the phase is opposite to the phase-bunched particles. The second order resonance condition is approximately fullfilled for these particles ($\mathrm{d}^2\Psi/\mathrm{d}t^2 \approx 0$), and they spend a long time in the separatrix region, which leads to noticeable pitch angle decrease (detailed analysis of the phase plane can be found in (Grach & Demekhov, 2018a)). The third regime is the particle trapping by the wave field, in which case the equatorial pitch angle also significantly decreases.

Nonlinear effects can also take place for $R \ge 1$. For low pitch angles and large K_μ in the case of $K_\mu > \mu$ quasi-linear estimate (7) won't apply (or will apply only for particles with certain initial phases). Force bunching (which is neglected in (7)) also becomes important for low Θ_L (small μ). If the wave amplitude is high enough, then the resonance point is shifted during the interaction, and in the case of strong dependence $K_\mu(\mu)$ that can cause drift in μ ($\langle\Delta\mu\rangle \neq 0$).

2.2 Wave packet model and plasma parameters

EMIC waves are observed in a wide range of geocentric distances L = 3–10 and longitudes 05–21 MLT (Anderson & Hamilton, 1993; Fraser & Nguyen, 2001; Loto'Aniu et al., 2005; Usanova et al., 2012; Keika et al., 2013). The frequencies of quasi-monochromatic wave packets (pearls or hydromagnetic chorus emissions) are in the range 1–3 Hz. Typical wave amplitudes are about 1–2 nT (Mursula, 2007; Engebretson et al., 2007; Engebretson et al., 2008), but values as large as 11 nT were observed (Engebretson et al., 2015).

In this paper, we consider the wave packets representing hydromagnetic chorus emissions with rising frequency, between the He^+ and proton gyrofrequencies (i.e., in the H^+ band).

The dipole model of geomagnetic field is used with McIlwain parameter $L = 5.69$. Cold plasma density at equator is $N_e = 30$ cm^{-3}, proton density at equator is $N_{H^+} = 0.95N_e$, helium and oxygen densities at equator are $N_{He^+} = N_{O^+} = 0.025N_e = 0.025N_e$.

The initial packet length is $L_{pt} \approx 4500$ km, the frequency grows linearly from $f_{fe} = 1.025$ Hz ($\approx 0.38 f_H$, where f_H is proton gyrofrequency) at the front edge to $f_{te} = 2.3$ Hz ($\approx 0.85 f_H$) at the trailing edge $z_{te} \approx -1$ km. As was shown by Kubota and Omura (2017); Grach and Demekhov (2018a, 2018b), the result of the resonance interaction can significantly depend on the amplitude profile. Like in (Grach & Demekhov, 2018a, 2018b), we also consider two initial profiles of the wave amplitude: constant (flat packet) and Gaussian-shaped (Gaussian packet) magnetic amplitude B_w. The maximum initial amplitude is chosen as $B_w^{max} = 3$ nT. The Gaussian shape seems more realistic, but we consider both shapes in order to demonstrate the nonlinear effects more clearly. The chosen parameters are typical for EMIC events observed by Van Allen Probes in H^+ band (e.g., (Engebretson et al., 2015)).

The packet propagates away from the equator (z increases). The evolution of the packet (in the cold plasma approximation) is taken into account in the simulation. The simulation time is limited to 6.5 s; at later times the dispersion distortion of the packet due to the presence of He^+ ions becomes significant. This choice of simulation time also allows us to neglect the effect of magnetic drift on the electron distribution function in a given flux tube. Indeed, the typical transverse size of EMIC wave packets known from spaceborne and ground-based measurements is about 2°. For the chosen energy range $W_0 = 1.4$–3.0 MeV, the drift time across the packet will be 17–36 s, which is more than two times longer than simulation time. The energy range is chosen based on R values for Gaussian packet (see below). The initial equatorial pitch angle range is $\Theta_{L0} = 7$–$80°$. From below it is limited by the loss cone (for $L = 5.69$, $\Theta_{Lc} \approx 5.8°$) and from above by the condition of the resonant interaction for particles within the specified energy range.

The system (2)–(5) was solved numerically by Bogacky-Shampine variant of the Runge-Kutta method. Calculations were done for 8 values of energy in the specified range (1.4; 1.6; 1.8; 2.0; 2.25; 2.5; 2.75 and 3.0 MeV), 74 values of equatorial pitch angle (step of 1 degree) and 180 values of the initial phase (uniformly in $[0, 2\pi]$). Thus, for every energy, the trajectories of 13320 particles were calculated. At the moment $t = 0$ all particles are placed at the trailing edge of the packet with positive longitudinal velocities. As is shown below, this is insignificant for the results, since the particles are spread over the field line in 3–4 bounces. If the particle is in the loss cone after leaving the packet ($\Theta_L < \Theta_{Lc}$), then the simulation for this particle is stopped.

3 Specific features of Interaction Regimes

3.1 Single pass through the wave packet

3.1.1 Inhomogeneity parameter

The resonance point locations and the unperturbed values of parameters R and K_μ for various initial equatorial pitch angles and the electron energies are shown in Figure 1 (for the initial packet location, $t = 0$). The values of K_μ are fairly large even for linear conditions ($R > 1$), which results from relatively low plasma density. The latter determines the EMIC wave refractive index entering formula (8).

The resonance point is shifted to the packet trailing edge with increasing Θ_L. For the flat wave packet, the inhomogeneity parameter R decreases with Θ_L and increases with energy W_0, while for the Gaussian wave packet R has a minimum in Θ_L which location depends on particle energy. Parameter K_μ has a maximum in Θ_L, but for the flat packet the K_μ decrease at high Θ_L is insignificant.

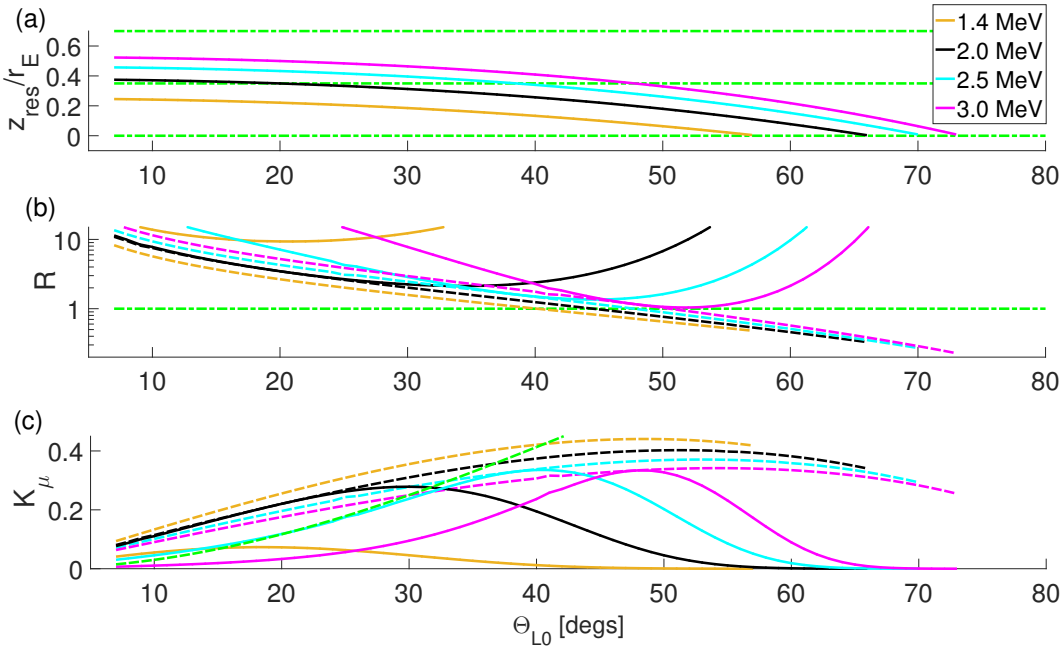

Figure 1. Resonance point location $z_{\rm res}$ normalized to the Earth radii $r_{\rm E}$ (a), unperturbed value of the inhomogeneity parameter R (b), and parameter K_μ (c) for the flat packet (dashed lines) and the Gaussian packet (solid lines). Green dash-dotted lines show the edges and middle of the packet (a), $R = 1$ (b) and the line $K_\mu = \mu$ (c).

Quantitatively, nonlinear regimes $R \leq 1$ for the Gaussian packet can be observed only for highest energies from the considered range and for a narrow pitch angle range near 50°. For the flat packet, $R \leq 1$ regimes can be observed for all energies, but for relatively high pitch angles $\Theta_L > 40°$. At the same time, as the dependence $K_\mu(\Theta_L)$ shows, various nonlinear effects are possible for $R > 1$ at low pitch angles, since the inequality $K_\mu > \mu$ is satisfied in a sufficiently wide pitch angle range (for all energies for the flat packet, for $W_0 < 2.75$ MeV for the Gaussian packet). For some pitch angles $|{\rm d}K_\mu/{\rm d}\Theta_{L0}|$ is relatively large, which means that nonlinear shift of the resonance point can be effective.

For Gaussian packet, propagation away from the equator shifts the location of minimum R to the lower Θ_L and increases its value (for illustration, see (Grach & Demekhov, 2018a)). Consecutively, R decreases for smaller Θ_L and increases for higher Θ_L. For the the flat packet, qualitatively the dependence on packet location is the same, but quantitatively it is much weaker.

Due to a fairly high wave amplitude and the packet being relatively short, the region of resonant interaction is determined by the effective packet length. Because of this, resonant interaction with packets with different profiles can yield different results even when resonance points are located in the middle of the packet (where R and K_μ are the same for both packets).

In (Grach & Demekhov, 2018a, 2018b) a similar wave packet was considered, but with a higher electron density $N_{\rm e}$. This leads to a higher refractive index n which in turn shifts the range of resonant electron energies to lower values and noticeably decreases R. In that case, nonlinear regimes $R \leq 1$ are also possible and effective for the Gaussian wave packet.

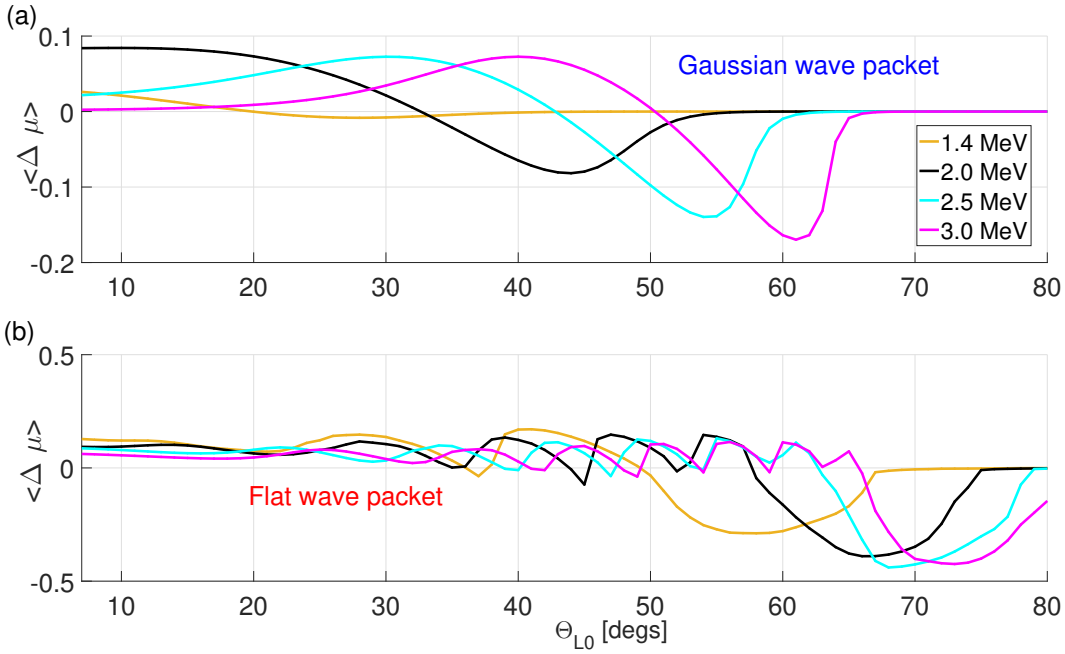

Figure 2. Phase averaged change in μ for the Gaussian (a) and flat (b) wave packets.

3.1.2 Change in pitch angle in different interaction regimes

The possibility and the comparative influence of various interaction regimes can be analyzed based on the phase averaged change of $\mu = \sin^2\Theta_L$. Dependencies $\langle\Delta\mu\rangle(\Theta_L, W_0)$ are shown in Figure 2.

According to Figure 2, various nonlinear regimes ($\langle\Delta\mu\rangle \neq 0$) are possible in a chosen range of parameters. Detailed analysis of particle trajectories shows the following.

For the Gaussian packet, positive $\langle\Delta\mu\rangle$ results from combined effect of force bunching and nonlinear shift of the resonance point under condition $\mathrm{d}K_\mu/\mathrm{d}\Theta_{L0} > 0$. Force bunching dominates for lower pitch angles, when the condition $K_\mu \geq \mu$ is satisfied for $R > 1$, i.e. quasi-linear estimate (7) formally allows pitch angle decrease to the negative values. Under these conditions, the force bunching (the second term on the right-hand side of (4), which is enhanced when $p_\perp \to 0$) ensures the physical consistence of the system (2)–(5) solution (the positivity of the first adiabatic invariant) and increases pitch angle during resonant interaction. For initial pitch angles near the loss cone, the influence of force bunching is so strong, that not only the mean value $\langle\Delta\mu\rangle > 0$, but also $\Delta\mu > 0$ for a single particle with an arbitrary initial phase. For this case, the particle trajectories, phase plane and $\Delta\mu(\Psi_{\mathrm{res}})$ are shown in Figure 3a. Note that the coefficients of the system (2)–(5) depend on time explicitly, i.e., the system is non-autonomous. Therefore, the trajectories on the phase plane may intersect (different trajectories reach the same point at different times). As one can see, resonance phase can take values from a limited range, and doesn't equal the phase at the point $\mathrm{d}\Psi/\mathrm{d}t = 0$.

In the case when the maximum of the $\langle\Delta\mu\rangle(\Theta_{L0})$ is located at the intermediate pitch angles ($W_0 > 2$ MeV), this maximum is caused by the nonlinear shift of the resonance point under condition $\mathrm{d}K_\mu/\mathrm{d}\Theta_{L0} > 0$. The negative values of $\langle\Delta\mu\rangle$ are caused by the nonlinear shift of the resonance point under condition $\mathrm{d}K_\mu/\mathrm{d}\Theta_{L0} < 0$, i.e. when change in pitch angle (7) decreases with Θ_{L0}. This case is illustrated by Figure 3b. As one can

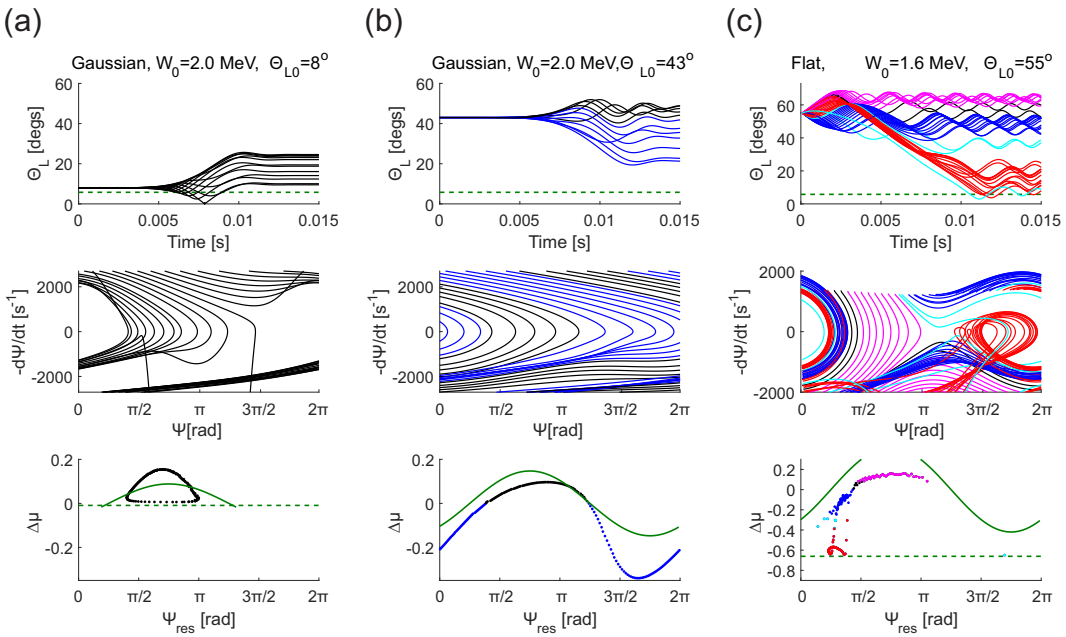

Figure 3. Illustration of the possible interaction regimes. Plots in columns a), b), and c) correspond, respectively, to the force bunching, nonlinear shift of the resonance point, and various regimes at $R < 1$. Top rows show the oscillograms of Θ_L, middle rows show the phase plane, and bottom rows show the $\Delta\mu$ dependence on the resonance phase. Colors denote types of particle trajectories: black and blue correspond to untrapped particles with $\Delta\mu > 0$ and $\Delta\mu < 0$, respectively, magenta to phase-bunched particles, cyan to directed scattering and red to wave trapping. Green dashed lines in the top and bottom rows indicate loss cone, and green solid lines correspond to quasi-linear estimate (7).

see, phase portrait of the system is close to the quasi-linear regime, while the dependence $\Delta\mu(\Psi_{\rm res})$ differs from estimate (7).

Nonlinear regimes corresponding to $R \leq 1$, i.e. phase bunching, directed scattering and particle trapping by the wave field occur for a certain fraction of particles for energies $W_0 \geq 2.5$ MeV in the vicinity of the minimum $\langle\Delta\mu\rangle$ (trapping only takes place for $W_0 = 3.0$ MeV).

For the flat packet, the region $\Theta_{L0} < 30$–$35°$ corresponds to the combined effect of force bunching and nonlinear shift of the resonance point under condition $\mathrm{d}K_\mu/\mathrm{d}\Theta_{L0} > 0$ (force bunching predominates for lower Θ_{L0}). For the intermediate pitch angles (from 30–50° for $W_0 = 1.4$ MeV to 40–65° for $W_0 = 3.0$ MeV), the main interaction regimes are phase bunching (causes local maximums $\langle\Delta\mu\rangle > 0$) and directed scattering (causes local minimums $\langle\Delta\mu\rangle \approx 0$). The smooth global minimum under high Θ_L is caused by the effective wave trapping, though for untrapped particles both phase bunching and directed scattering can take place. This case is shown in Figure 3c. The global minimum of the dependence $\langle\Delta\mu\rangle(\Theta_L)$ for the flat packet corresponds to the unperturbed resonance point located at the trailing edge of the packet. At higher pitch angles, the unperturbed resonance condition is not fulfilled within the packet, but due to a nonlinear shift of the resonance point, for some particles the resonance condition can be fullfilled; all such particles are trapped by the wave field. Detailed study of the nonlinear interaction regimes under $R < 1$ can be found in (Grach & Demekhov, 2018a, 2018b).

For both packets, increasing of the electron energy shifts $\langle\Delta\mu\rangle(\Theta_L)$ to the higher Θ_L. Wave packet propagation away from the equator will shift $\langle\Delta\mu\rangle(\Theta_L)$ to the lower Θ_L (same as with $R(\Theta_L), K_\mu(\Theta_L)$).

3.2 Precipitation mechanisms and effects of wave packet propagation

Preliminary analysis of particle trajectories shows that precipitation is possible as a result of either almost quasi-linear interaction, directed scattering or wave trapping. The range of particle pitch angles for which the precipitation in either regime is possible is also influenced by force bunching, nonlinear shift of the resonance point and phase bunching. To study the role of each precipitation mechanism we plot temporal dynamics of 'scattering' equatorial pitch angle $\Theta_{L\rm sc}$ defined as equatorial pitch angles of precipitated electrons before the last interaction. Similar analysis was made by Kubota and Omura (2017), for different wave packet and plasma parameters, but they did not discuss the precipitation for the particles near the loss cone. We also show the distribution of all precipitated particles over $\Theta_{L\rm sc}$.

3.2.1 Gaussian wave packet

The results for the Gaussian wave packet are shown in Figure 4. For the first 3–4 passes of particles through the wave packet in the resonant direction (which takes about 2 s) the temporal dynamics is influenced by the initial particle distribution in space. Recall that at $t = 0$, the ensemble of the particles is placed at the trailing edge of the wave packet. After that, the particles can be considered uniformly distributed between the mirror points. The initial particle location doesn't influence the distribution of precipitated particles over the scattering pitch angles.

The precipitation is possible only for $\Theta_{L\rm sc} \leq 35°$. For these values, three regimes are possible: almost quasi-linear regime, force bunching, and nonlinear shift of the resonance point with $\langle\Delta\mu\rangle > 0$. Nonlinear resonance shift with $\langle\Delta\mu\rangle < 0$ takes place only for $\Theta_L \geq 40°$, which is above $\Theta_{L\rm sc}$ range. That means that precipitation in this regime is not possible, but particles can be effectively moved to the lower pitch angles (see also Figure 3b). As it was mentioned above in Section 3.1.2, the nonlinear regimes under $R \leq 1$ take place only for a small fraction of particles and do not have significant effect.

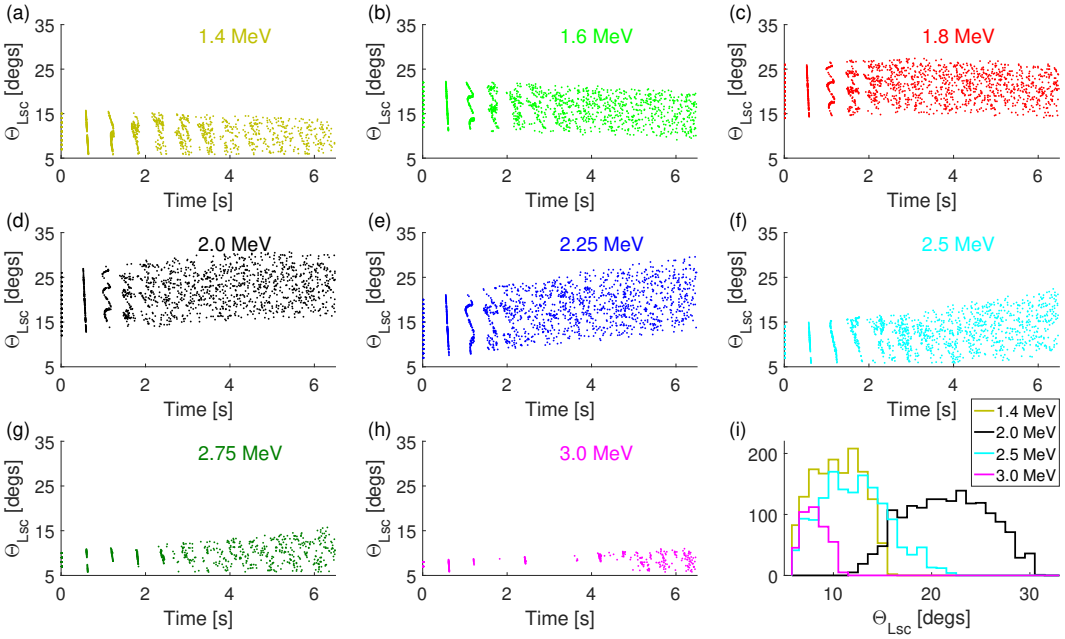

Figure 4. Equatorial pitch angles Θ_{Lsc} of precipitated electrons before the last interaction with the wave packet as a function of time, for the Gaussian wave packet. Time stamps correspond to particle exiting the wave packet, i.e. approximately a one and a quarter of bounce period T_B before precipitating. Panel (i) shows the distribution of precipitated particles over Θ_{Lsc} during the entire simulation interval.

For particles with energies 1.6–2.5 MeV, the influence of force bunching is strong enough to block precipitation completely for equatorial pitch angles up to $\Theta_L \approx 15°$.

The range of Θ_{Lsc} depends on time for most of the energies. For lower energies, $W_0 = 1.4$–1.6 MeV, resonance points for $\Theta_L < 25°$ at $t = 0$ are located closer to the trailing edge of the packet and for them R increases and K_μ decreases as the packet propagates (at the time $t = 0$, minimum R is located close to the loss cone). Smaller values of K_μ correspond to lower initial pitch angles for which estimate (7) gives decreasing of μ below the loss cone value μ_c (precipitation in quasi-linear regime) or below zero (effective force bunching blocking precipitation). Thus, both maximum and minimum Θ_{Lsc} decrease in this case. For higher energies, $W_0 = 2.0$–3.0 MeV, the situation is the opposite: resonance points for $\Theta_L < 25°$ at $t = 0$ are located closer to the front edge of the packet, thus R decreases (K_μ increases) as wave packet propagates. Thus, both maximum and minimum values of Θ_{Lsc} increase.

Distributions of precipitated particles over Θ_{Lsc} (Figure 4i) have similar profiles for all the energies, i.e., they have a smooth maximum in the middle of the Θ_{Lsc} range.

3.2.2 Flat wave packet

The temporal dynamics of Θ_{Lsc} is shown in Figure 5.

For all energies, there is a small number of particles which are scattered into loss cone having initial pitch angle that differs from Θ_{Lc} by fractions of a degree. The analysis of their trajectories shows that these particles precipitate after non-resonant interaction with the wave packet (due to the large amplitude) to conjugated ionosphere. Their

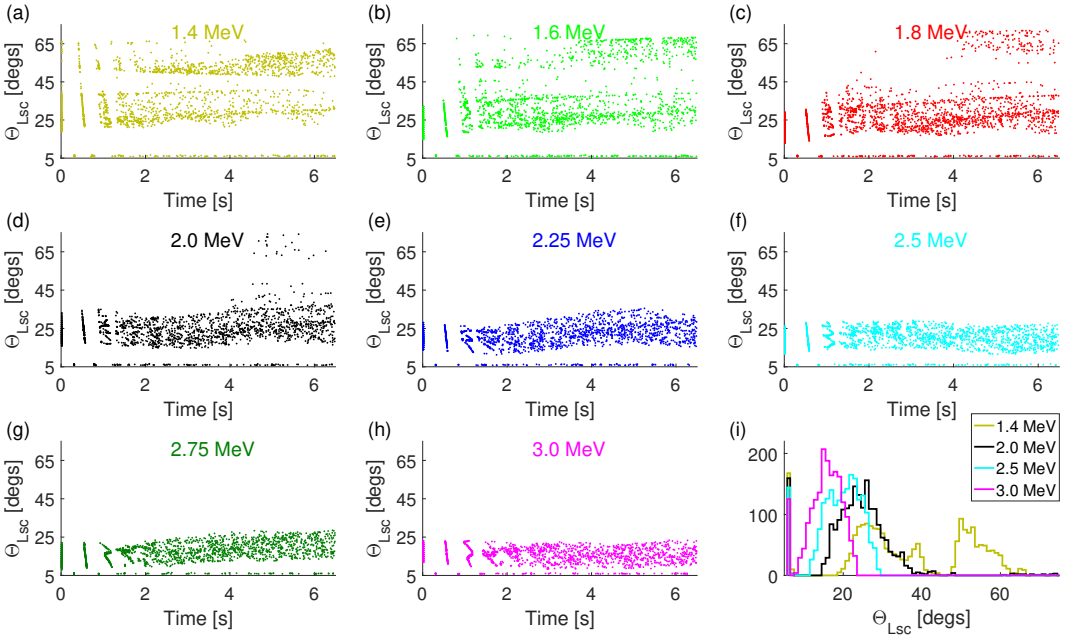

Figure 5. Same as in Figure 4, but for the flat packet.

number is small compared to the total number of precipitated particles, and they do not influence any further results.

Force bunching blocks precipitation from low pitch angles for all energies, though its influence (range of 'blocked' pitch angles) decreases with energy and varies with time. Scattering pitch angles $\Theta_{Lsc} < 45$–$50°$ correspond to precipitation after almost quasi-linear interaction or directed scattering. High scattering pitch angles correspond to precipitation directly caused by wave trapping. This effect is possible only for energies $W_0 =$ 1.4–2.0 MeV; with increasing energy this precipitation starts later in time. It can be explained as follows. For higher energies, the region of effective wave trapping is located at higher Θ_L (see Figure 2b), thus even the same value of $\langle \Delta\mu \rangle$ is not enough for a particle to precipitate. Wave packet propagation shifts the effective wave trapping region to lower pitch angles, which makes precipitation possible.

Distributions of precipitated particles in pitch angles have different profiles for different energies. Apart from the very narrow maximum very close to the loss cone, which corresponds to the particles precipitated after non-resonant interaction, their structure is as follows. For $W_0 = 1.4$–1.8 MeV, the distributions have three local maxima: the first one (near 20°) corresponds to quasi-linear regime, and the second (around 40°) and third (50–70°) ones correspond to directed scattering and wave trapping, respectively. The 'dip' between the second and the third maxima can also be seen on the temporal dynamics panels. It corresponds to the region where phase bunching prevails (recall that phase bunching results in a pitch-angle increase). For energies $W_0 = 2.0$–3.0 MeV, precipitation is mostly caused by quasi-linear regime, though precipitation by directed scattering is also possible for a number of particles.

The smooth variations of scattering pitch angle range (for quasi-linear regime) are connected with fluctuations in $\langle \Delta\mu \rangle(\Theta_L)$; wave packet propagation will shift the local extrema of $\langle \Delta\mu \rangle(\Theta_L)$.

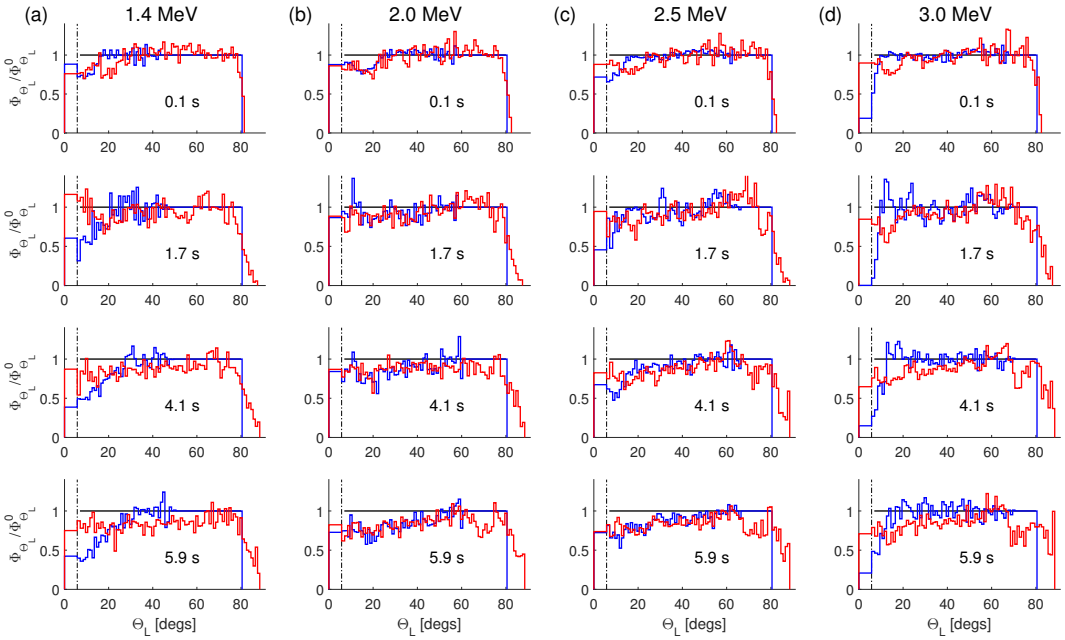

Figure 6. The evolution of pitch angle distribution for the Gaussian packet (blue lines) and the flat packet (red lines). Solid black line shows the initial distribution $\Phi_{\Theta_L}|_{t=0} = \text{const} = \Phi^0_{\Theta_L}$, dash-dotted black line indicates Θ_{Lc}.

4 Pitch Angle Distribution and Precipitation Fluxes

In the further analysis of the simulation results, the total simulation time 6.5 s is divided into 11 intervals $\{\Delta t_i\} = t_{i+1} - t_i$, $i = 0, 1, ..11$, $t_0 = 0$, where $\Delta t_0 = 0.2$ s and the subsequent intervals $\Delta t_{0<i<11} = 0.6$ s. The latter value corresponds to the bounce period of particles close to the loss cone: $T_{\rm B}(\Theta_L = \Theta_{Lc}) \approx 0.6$–$0.64$ s. Since at the initial time $t = 0$ all electrons are located at the trailing edge of the wave packet, the first time interval $\Delta t_0 = 0.2$ s was chosen sligthly longer than the time $T_{\rm B}(\Theta_L = \Theta_{Lc})/4 \approx 0.15$ s after which a particle near the loss cone reaches the ionosphere. Since $\Delta t_0 < T_{\rm B}(\Theta_L = 80°) \approx 0.33$ s we can say that during Δt_0 all particles passed the wave packet in resonant direction only once. We average the particle distribution function and the precipitation flux over the intervals Δt_i and attribute the obtained result to the time $T_i = (t_{i+1} + t_i)/2$ (the middle of the interval Δt_i).

To analyze the simulation results in terms of particle distribution function and to compare obtained precipitation fluxes with quasi-linear estimates, we have to establish the connection between the distribution function $\Phi_{\Theta_L}(\Theta_L)$ (or $\Phi_\mu(\mu)$) and the distribution of the test particles in the phase space. This procedure is described in detail in the Appendix.

4.1 Evolution of pitch angle distribution

The particles distribution function $\Phi_{\Theta_L}(\Theta_L)$ for both wave packets for several energy values at several times T_i is shown in Figure 6.

For the flat packet, the distribution function dynamics is qualitatively similar for all the energies considered. For the low equatorial pitch angles near the loss cone, the distribution function is either close to isotropic (with a value slightly lower than the initial value $\Phi^0_{\Theta_L}$; this value decreases slightly with increasing energy), or it has a local max-

imum in the loss cone. In most cases, the global maximum of the distribution function is located at the pitch angles 60–70° and is equal to the initial value $\Phi_{\Theta_L}(\Theta_L)$ or slightly exceeds it.

For the Gaussian packet, for intermediate energies $W_0 = 1.8$–2.25 MeV and not high pitch angles $\Theta_L \leq 60°$ the distribution function almost coincides with the distribution function for the flat packet. For lower energies $W_0 = 1.4$–1.6 MeV, this statement is valid in the beginning of the simulation, and for energy $W_0 = 2.5$ MeV it is valid for late times. The similar behavior of distribution functions for both packets corresponds to the resonance points for particles with intermediate pitch angles located in the middle of the wave packet. It also agrees with the dynamics of the scattering pitch angles shown in Figure 4 (as wave packet propagates, scattering pitch angle range decreases for $W_0 = 1.4$–1.6 MeV and increases for $W_0 = 2.5$ MeV).

At late times for energies 1.4–1.6 MeV and initial times for $W_0 = 2.5$ MeV, the distribution function smoothly increases from a value $\Phi^{\rm c}_{\Theta_L}$ in the loss cone to the initial value at pitch angles $\Theta_L = 30$–$40°$; the value of $\Phi^{\rm c}_{\Theta_L}$ is not small. For higher energies 2.75–3.0 MeV, the distribution function abruptly increases from small value $\Phi^{\rm c}_{\Theta_L}$ to the initial value $\Phi^{0}_{\Theta_L}$ at pitch angles $\Theta_L \approx 15$–$20°$. For higher pitch angles, Φ_{Θ_L} fluctuates.

The main difference between the the flat and Gaussian wave packets is observed for high pitch angles $\Theta_L > 60°$, because for this range the resonance points are located near the trailing edge of the packet. For Gaussian packet, due to the small amplitude there is no resonant interaction for these pitch angles, and the distribution function remains constant. For the flat packet, firstly, small fluctuations of Θ_L are possible even when the exact resonance condition is not fulfilled within the packet, and secondly, due to nonlinear shift of the resonance point, a fraction of particles may be trapped by the wave field, which results in large pitch angle decrease and leads to the appearance of 'dips' in the distribution function in the corresponding region.

4.2 Precipitation fluxes

To analyze the precipitation fluxes $S^{\rm num}_{\rm pr}$, directly corresponding to the numerical simulation results, we normalize them to the flux $S^{\rm SD}_{\rm pr}$ in the limiting case of strong diffusion. In this case the loss cone is filled continuously and distribution function is isotropic; the precipitation flux takes the limiting value equal to the trapped flux (Kennel & Petschek, 1966; Bespalov & Trakhtengerts, 1986; Trakhtengerts & Rycroft, 2008):

$$S^{\rm SD}_{\rm pr} = \frac{N\mu_{\rm c}}{\overline{T}_B}. \tag{11}$$

Here N is the total number of particles in geomagnetic field tube with unit cross section at the ionosphere, $\overline{T}_B = \int T_{\rm B}(\mu){\rm d}\mu$, $\mu_{\rm c}$ corresponds to the loss cone.

In the case when distribution function $\Phi_\mu(\mu)$ is not isotropic and doesn't have maximum in the loss cone (i.e., has a finite positive derivative $\partial\Phi_\mu/\partial\mu$), it is possible to obtain quasi-linear estimates of precipitation fluxes $S^{\rm lin}_{\rm pr}$. For this, we use the smooth approximation $\Phi^{\rm sm}_\mu(\mu)$ of numerically obtained distribution function. The root mean square deviation of μ that determines the diffusion coefficient is calculated using both the analytical estimate (10) and numerical results (A15). Calculation algorithms for both $S^{\rm num}_{\rm pr}$ and $S^{\rm lin}_{\rm pr}$ can be found in the Appendix.

Since for the flat packet the distribution function is either close to isotropic or has a local maximum in the loss cone, quasi-linear estimates of precipitation flux $S^{\rm lin}_{\rm pr}$ were calculated only for the Gaussian packet and only for those times when the derivative of the distribution function in the vicinity of loss cone was not close to zero.

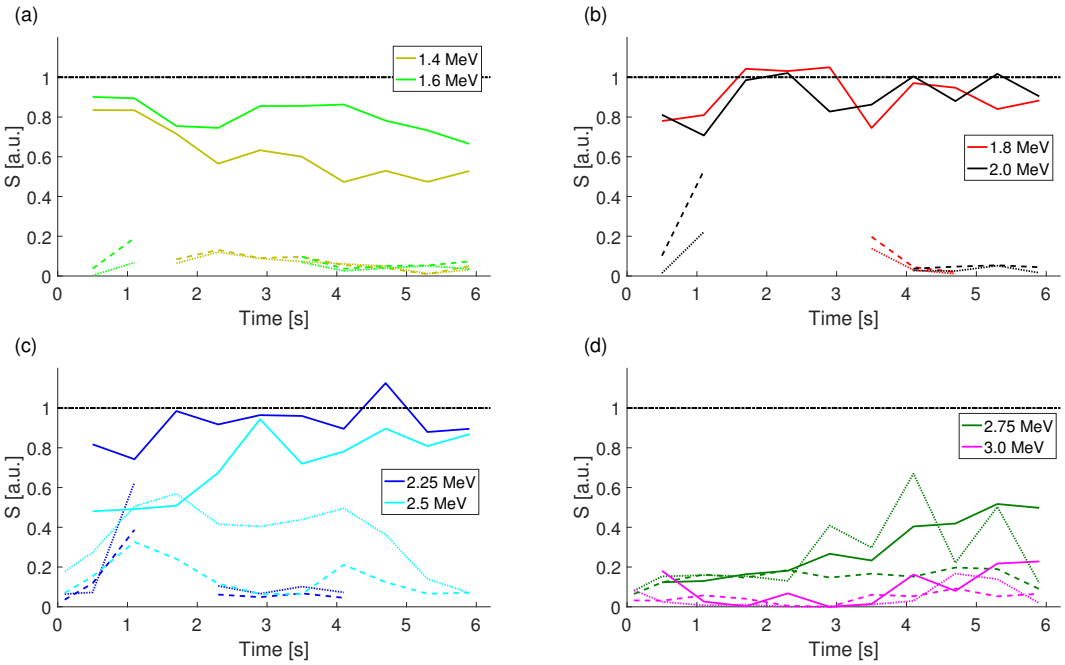

Figure 7. Precipitation fluxes for the Gaussian packet: normalized precipitation flux $S_{\rm pr}^{\rm num}/S_{\rm pr}^{\rm SD}$ (solid lines) and quasi-linear flux $S_{\rm pr}^{\rm lin}/S_{\rm pr}^{\rm SD}$, calculated using diffusion coefficient based on theoretical estimate (10) (dashed lines) and simulation results (A15) (dotted lines).

The normalized precipitation fluxes are shown in the Figures 7 and 8. Numerical fluxes $S_{\rm pr}^{\rm num}$ are calculated for intervals starting from moment $t_1 = 0.2$ s, to avoid the influence of the initial spatial distribution of the particles. Precipitation fluxes, averaged over simulation time, are shown in Figure 9.

The dynamics of precipitation fluxes corresponds to the dynamics of the distribution function. For the flat packet, the flux $S_{\rm pr}^{\rm num}$ fluctuates near the limiting flux $S_{\rm pr}^{\rm SD}$: $S_{\rm pr}^{\rm num} = (0.8\text{–}1.4)S_{\rm pr}^{\rm SD}$. The fluxes exceeding the limiting value correspond to nonmonotonic distribution function having a local maximum in the loss cone.

The largest values of $S_{\rm pr}^{\rm num}/S_{\rm pr}^{\rm SD}$ (both maximum and time-averaged) correspond to the energy 1.4 MeV, the smallest ones correspond to 3.0 MeV. For intermediate energies, the dependence of maximum/minimum and average fluxes on the energy is nonmonotonic (see Figure 9). Such a dependence clearly indicates the competition between two nonlinear regimes, which have opposite effects on pitch angle dynamics, but the same energy dependence. Recall that force bunching blocks the precipitation from low pitch angles, while wave trapping can directly cause precipitation from high pitch angles; the influence of both regimes decreases with increasing energy.

For the Gaussian packet, dependence of normalized flux $S_{\rm pr}^{\rm num}/S_{\rm pr}^{\rm SD}$ on energy and time is much stronger. The maximum values of $S_{\rm pr}^{\rm num}/S_{\rm pr}^{\rm SD}$ correspond to intermediate energies $W_0 = 1.8$–2.25 MeV. In this case, like in the case of the flat packet, $S_{\rm pr}^{\rm num}$ fluctuates near $S_{\rm pr}^{\rm SD}$, though its values are smaller: $S_{\rm pr}^{\rm num} = (0.7\text{–}1.1)S_{\rm pr}^{\rm SD}$. For lower energies $W_0 = 1.4$–1.6 MeV the normalized precipitation flux increases with energy and decreases with time; for higher energies $W_0 = 2.5$–3.0 MeV the situation is the opposite. This temporal dynamics and dependence on energy follows the dynamics of resonant interaction effectiveness (the value of R) at low ('scattering' range) pitch angles.

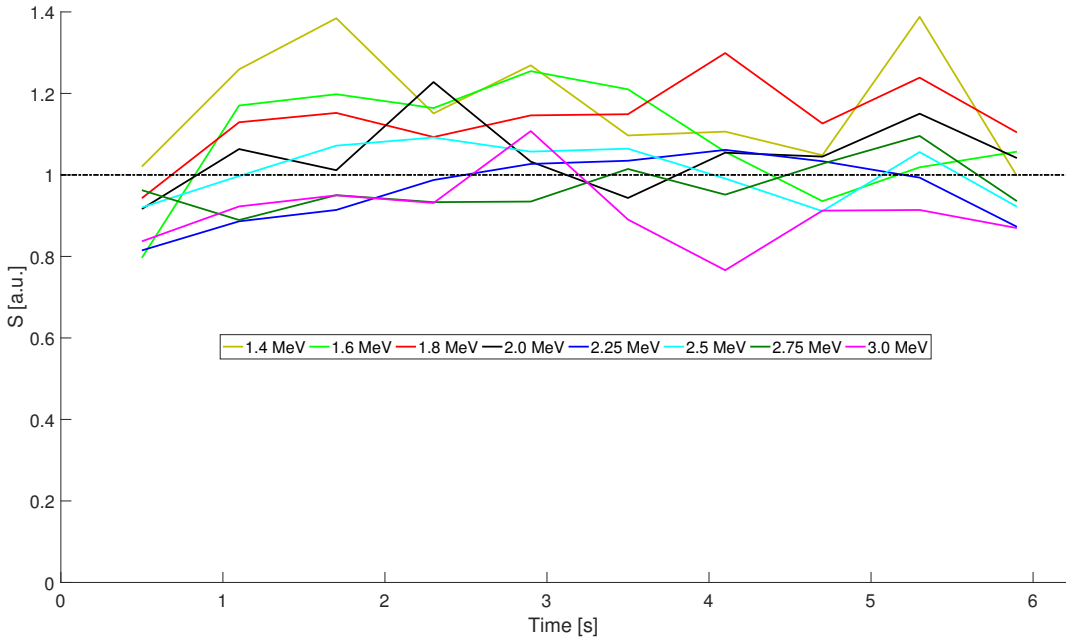

Figure 8. Normalized precipitation fluxes $S_{\rm pr}^{\rm num}/S_{\rm pr}^{\rm SD}$ for the flat packet.

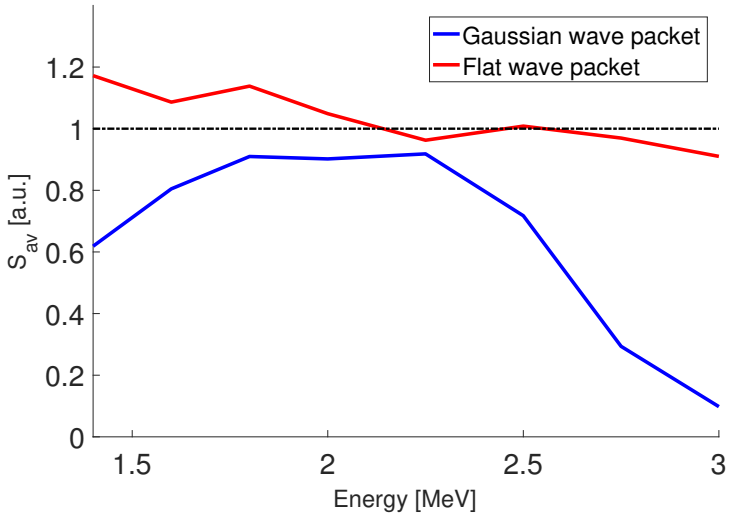

Figure 9. Normalized precipitation fluxes, averaged over the simulation time, for the flat (red line) and Gaussian (blue line) wave packets.

In most cases, analytical and numerical values of the root mean square change in μ ((10) and (A15), respectively) are close to each other (see Figure A2). That means that theoretical estimate (10) can be valid even in the case of strong nonlinear effects and $\langle \Delta\mu \rangle \neq 0$. Correspondingly, quasi-linear estimates of the precipitation flux obtained by using either (10) or (A15) give similar results. In contrast to this fact, the fluxes $S_{\rm pr}^{\rm lin}$ are close to the 'numerical' flux $S_{\rm pr}^{\rm num}$ only for energies $W_0 = 2.75$–3.0 MeV and for initial times for $W_0 = 2.5$ MeV. For lower energies, $S_{\rm pr}^{\rm lin} \ll S_{\rm pr}^{\rm num}$. The low values of quasi-linear estimates are caused by the following. The smoothed distribution function, which is used for calculating the quasi-linear precipitation flux (see Appendix, Figure A1), in these cases is virtually isotropic, while the original distribution function, obtained in the simulation, has a local maximum in the loss cone, which can't be described by the diffusion equation.

It's interesting to note that for lower energies $W_0 = 1.4$–1.6 MeV, when Φ_μ increases monotonically from the loss cone, quasi-linear estimates are also much smaller than the numerical fluxes obtained directly from the simulation results. Most likely, it is explained by the following factors. Quasi-linear estimates for the precipitation flux are obtained by the averaging over bounce oscillations; this approach can be used when change in μ during one bounce period (as a result of one resonant interaction) is relatively small. With considered parameters of plasma and wave packets, for energies $W_0 < 2.75$ MeV and low pitch angles (scattering pitch angles range) $\Delta\mu \sim \mu$ and overall number of bounce oscillations is not large. In this case, averaging over bounce oscillations can lead to incorrect results.

5 Discussion and Conclusions

The precipitation fluxes are formed as a result of several interaction regimes with opposite effects. The influence of each regime depends on wave packet characteristics and electron energy.

Under considered parameters of plasma and wave packets, particle trapping by the wave field is not very effective, but the role of nonlinear regimes with inhomogeneity parameter $R \geq 1$ is significant.

The effect of force bunching (the influence of Lorentz force on the particle phase) on the resonant interaction is rarely discussed in analytical studies. Lundin and Shkliar (1977) analyzed motion of resonance electrons with low transverse velocities in the field of a whistler mode parallel propagating wave. They showed that when wave amplitude is high enough, force bunching leads to systematic increase in electron pitch angle. Our simulation shows similar results for electrons interacting with EMIC waves: force bunching leads to pitch angle increase for particles with very low pitch angles near the loss cone. In most part of the considered energy range ($W_0 = 1.6$–2.25 MeV for the Gaussian wave packet and $W_0 < 3$ MeV for the flat wave packet) force bunching blocks the precipitation completely from a noticeable range of equatorial pitch angles (up to 15° and 25° for the Gaussian and flat wave packets, respectively). The significance of the force bunching influence is connected with a relatively low electron plasma density; the latter results in low refractive index, which in turn leads to large change in equatorial pitch angle when $R > 1$ and trapping by the wave field is not possible. Under different plasma conditions, as reported by Kubota and Omura (2017), force bunching can lead to strong equatorial pitch angle decrease for particles released from the wave trapping.

Shift of the resonance point is another nonlinear effect which is important under considered conditions when $R > 1$. For low equatorial pitch angles $\Theta_L \leq 30$–$40°$, nonlinear shift of the resonance point leads to an average increase of the pitch angle. For higher pitch angles, this effect takes place only for the Gaussian wave packet and has the opposite sign, i.e. pitch angle decreases. This decrease does not directly cause precip-

itation, but particles can be moved to the pitch angles where almost quasi-linear diffusion takes place and precipitation occurs.

Three nonlinear regimes are possible for inhomogeneity parameter $R < 1$: phase bunching (pitch angle increase for a large number of untrapped particles), directed scattering (strong pitch angle decrease for a small number of untrapped particles) and particle trapping by the wave field (also leads to pitch angle decrease in our case). For the Gaussian wave packet and considered parameters, these regimes are possible only for higher energies 2.75–3.0 MeV and in a narrow range of pitch angles, so they do not play a significant role. For the flat wave packet, precipitation as a result of directed scattering and wave trapping is possible for $W_0 = 1.4$–2.0 MeV. For higher energies, directed scattering and wave trapping move particles to the pitch angle range of quasi-linear scattering. Phase bunching blocks precipitation from intermediate equatorial pitch angles and moves particles into the region of effective wave trapping.

It is important to note that, even when the nonlinear precipitation is most effective (flat packet, $W_0 = 1.4$ MeV, see Figure 5), the number of 'nonlinearly' precipitated particles doesn't exceed the number of the particles precipitated in almost quasi-linear regime. The situation will be different for a plasma with higher cold electron density (Kubota & Omura, 2017; Grach & Demekhov, 2018a, 2018b), when the inhomogeneity parameter takes smaller values, and directed scattering and wave trapping are more effective. In that case, nonlinear precipitation will be possible for a Gaussian wave packet (Grach & Demekhov, 2018a, 2018b), and precipitation fluxes will be formed mostly by combined effect of wave trapping and directed scattering (Kubota & Omura, 2017).

To analyze the precipitation fluxes, we have normalized the precipitation fluxes to the flux value in the case of strong diffusion, which corresponds to continuous filling of the loss cone, i.e. isotropic distribution function in the vicinity of the loss cone. Maximum normalized fluxes (the whole energy range for the flat packet, $W_0 = 1.8$–2.25 MeV for the Gaussian packet) are close in value and fluctuate near strong diffusion flux. In these cases, distribution function in the vicinity of the loss cone is close to isotropic; there are also moments in which distribution function has a maximum in the loss cone.

For the flat packet, the normalized flux averaged over the simulation time globally decreases with energy, but the dependence is nonmonotonic. This nonmonotonic dependence results from the competition of nonlinear regimes with mutually opposite effects (force bunching and wave trapping) whose strength decreases with energy.

For the Gaussian packet, the time-averaged normalized flux has a maximum over energy. The stronger dependence on particle energy for the Gaussian packet is caused by the different amplitude values at different resonance points. Maximum normalized fluxes are reached for $W_0 = 1.8$–2.25 MeV; in this case, the resonance points for particles with 'scattering' pitch angles are located near the middle of the packet. For lower energies ($W_0 = 1.4$–1.6 MeV) the resonance points for 'scattering' particles are located near the trailing edge of the packet. In this case, the normalized fluxes decrease with time and increase with energy. For higher energies 2.5–3.0 MeV (the resonance points for 'scattering' particles are located near the front edge of the packet) the situation is the opposite. The temporal dynamics and energy dependence of the precipitation fluxes and 'scattering' pitch angles range for lower and higher energy follows the dynamics of inhomogeneity parameter R at low ('scattering' range) pitch angles.

We have compared the precipitation fluxes, obtained in the simulation, with theoretical quasi-linear estimates. For the parameters where quasi-linear equations for the distribution function are applicable, the numerical fluxes are close to theoretical estimates. This is true for higher energies ($W_0 = 2.75$–3.0 MeV) for the Gaussian packet. In other cases, including the ones where precipitation fluxes are formed under $R \geq 1$, i.e., when

no trapping is possible, numerical precipitation fluxes exceed theoretical estimates by a factor from 2 to more than 10.

In conclusion, we briefly summarize the main results of this study.

1. The influence of Lorentz force on the particle phase (force bunching) can completely block the precipitation from low equatorial pitch angles.
2. For the major part of the considered parameter domain, the pitch angle distribution is close to isotropic in the vicinity of the loss cone.
3. The precipitation fluxes are formed as a result of several interaction regimes with opposite effects. For higher energies (2.75–3.0 MeV in the considered case), theoretical quasi-linear estimates are applicable, and the numerical fluxes are close to them. For lower energies, numerical precipitation fluxes exceed theoretical estimates by a factor from 2 to more than 10. This result is important for using quasi-linear diffusion fluxes in numerical modelling of radiation belts.

Appendix A Calculation of the Pitch Angle Distribution Function and Precipitation Fluxes

Most of the expressions below follow (Bespalov & Trakhtengerts, 1986; Trakhtengerts & Rycroft, 2008) and are given here for the reader's benefit.

Let f be the particle distribution function averaged over gyrophases. If the pitch angle and energy change during one bounce oscillation is not very large, then the distribution function F averaged over bounce oscillation period T_B is close to the local distribution function f:

$$F = \frac{1}{T_\mathrm{B}} \int f \mathrm{d}t \approx \frac{1}{T_\mathrm{B}} \int f \frac{\mathrm{d}z}{v_{||}} \approx f. \tag{A1}$$

Total number of particles in a geomagnetic flux tube with unit cross section at the ionosphere can be calculated as

$$N = \int n(z) \frac{B_{0\mathrm{m}}}{B_0(z)} \mathrm{d}z. \tag{A2}$$

Here $n(z) = \int f d^3\mathbf{p} = \int f \sin\Theta \mathrm{d}\Theta\, p^2 \mathrm{d}p\, \mathrm{d}\Psi$ is the local number density, Θ is the local pitch angle, and $B_{0\mathrm{m}}$ is the maximum field for the given geomagnetic field line.

From expressions (A1) and (A2) we can obtain:

$$N = \frac{1}{2\mu_\mathrm{c}} \int 2T_\mathrm{B} F_{\Theta_L}(\Theta_L) \cos\Theta_L \sin\Theta_L \mathrm{d}\Theta_L\, p^2 \mathrm{d}p\, \mathrm{d}\Psi = \frac{1}{2\mu_\mathrm{c}} \int T_\mathrm{B} F_\mu(\mu) \mathrm{d}\mu\, p^2 \mathrm{d}p\, \mathrm{d}\Psi. \tag{A3}$$

Here F_{Θ_L} is the distribution function F written as a function of Θ_L and F_μ is the distribution function F written as a function of μ: $F_{\Theta_L}(\Theta_L) = F_\mu(\mu = \sin^2\Theta_L)$. The value $\mu_\mathrm{c} = \sin^2\Theta_{Lc} = B_{0L}/B_{0\mathrm{m}}$ corresponds to the loss cone.

The particle energy change during the resonant interaction with EMIC waves is insignificant, so we can consider particles with $W_0 = \mathrm{const}$. Then we can use for every energy:

$$F = \frac{\delta(p-p_0)}{p_0^2} \widetilde{F}_{\Theta_L}(\Theta_L, \Psi) = \frac{\delta(p-p_0)}{p_0^2} \widetilde{F}_\mu(\mu, \Psi), \tag{A4}$$

where p_0 is the particle momentum. Integrating (A3) over Ψ and p with account of (A4), we obtain

$$N = \frac{v_0}{2\mu_\mathrm{c}} \int \widetilde{\Phi}_{\Theta_L} T_\mathrm{B} 2 \cos\Theta_L \sin\Theta_L \mathrm{d}\Theta_L = \frac{v_0}{2\mu_\mathrm{c}} \int \widetilde{\Phi}_\mu T_\mathrm{B} \mathrm{d}\mu. \tag{A5}$$

Here $v_0 = p_0/(m\gamma)$,

$$\widetilde{\Phi}_{\Theta_L} = \int \widetilde{F}_{\Theta_L}(\Theta_L, \Psi) \mathrm{d}\Psi; \quad \widetilde{\Phi}_\mu = \int \widetilde{F}_\mu(\mu, \Psi) \mathrm{d}\Psi. \tag{A6}$$

In order to connect the number $N_{\rm p}$ of particles in the simulation with N, we use the following normalization:

$$N = \frac{v_0 \overline{T}_B}{2\mu_{\rm c}} \beta_{\rm V} N_{\rm p}, \tag{A7}$$

where $\overline{T}_B = \int T_{\rm B}(\mu){\rm d}\mu$, $\beta_{\rm V}$ is the normalization constant, and $N_{\rm p}$ is the number of particles in the simulation.

Using (A7), we can write the connection between distribution functions $\widetilde{\Phi}_\mu$ and $\widetilde{\Phi}_{\Theta_L}$ and distribution of the test particles in the phase space as follows:

$$\widetilde{\Phi}_{\Theta_L} = \frac{\Delta N_{\rm p}}{\Delta\Theta_L} \frac{\overline{T}_B}{T_{\rm B}} \frac{\beta_{\rm V}}{\sin(2\Theta_L)}; \tag{A8}$$

$$\widetilde{\Phi}_{\mu} = \frac{\Delta N_{\rm p}}{\Delta\mu} \frac{\overline{T}_B}{T_{\rm B}} \beta_{\rm V}. \tag{A9}$$

Here $\Delta N_{\rm p}$ is the number of particles having the pitch angle Θ_L within the range $\Delta\Theta_L$ (in (A8)) and μ in the range of $\Delta\mu$ (in (A9)).

If the initial distribution of test particles in Θ_L is uniform and equal weight is assigned to each particle, then initial distribution function $\widetilde{\Phi}_{\Theta_L}|_{t=0}$ is not constant. At the same time, each particle corresponds to the phase space element $\Delta\Gamma = \sin(2\Theta_L)\Delta\Theta_L\Delta\Psi = \Delta\mu\Delta\Psi$, which does not change during the distribution function evolution. For a more correct analysis of simulation results, instead of the initial function $\widetilde{\Phi}_{\Theta_L}|_{t=0}$ we use the 'weighted' distribution function $\Phi_{\Theta_L}|_{t=0} = \alpha_{\rm w}(\Theta_{L0})\widetilde{\Phi}_{\Theta_L}|_{t=0} = {\rm const}$, where $\alpha_{\rm w}(\Theta_{L0})$ are the weights assigned to each particle with initial equatorial pitch angle Θ_{L0}. The weights are calculated from the condition that the functions $\Phi_{\Theta_L}|_{t=0}$ and $\widetilde{\Phi}_{\Theta_L}|_{t=0}$ have the same normalization.

To analyze the simulation results we divide the pitch angle values, corresponding to the moments $t_{i+1} < t \le t_i$, $0 \le i \le 11$ into the intervals $\Delta\Theta_{L\,k}$ ($\Delta\Theta_{L\,1} = \Theta_{Lc}, \Delta\Theta_{L\,1,2,\ldots} = 1^\circ$). Every particle is counted with the weight $\alpha_{\rm w}(\Theta_{L0})$, corresponding to its initial equatorial pitch angle Θ_{L0}. To obtain the value of the distribution function in the loss cone, we count the particles which were scattered in the loss cone during the current time interval Δt_i. The obtained distribution function is attributed to the time $T_i = (t_{i+1} + t_i)/2$.

The effect of quasi-linear pitch angle diffusion on the averaged distribution function is described by the following equation (Bespalov & Trakhtengerts, 1986; Trakhtengerts & Rycroft, 2008):

$$\frac{\partial F_\mu}{\partial t} = \frac{1}{T_{\rm B}} \frac{\partial}{\partial\mu} \left[\mu \overline{D} \frac{\partial F_\mu}{\partial\mu} \right]. \tag{A10}$$

Here $\overline{D} = \int D{\rm d}t = \int D{\rm d}s/v_{||}$, D is the diffusion coefficient, and the integral is taken over the interval of bounce averaging. The diffusion coefficient is calculated as

$$D = \frac{(\langle\Delta\Theta_L\rangle_{\rm rms})^2}{\Delta t}. \tag{A11}$$

Here $\langle\Delta\Theta_L\rangle_{\rm rms} = \sqrt{\langle(\Delta\Theta_L - \langle\Delta\Theta_L\rangle)^2\rangle}$ is the root mean square deviation of Θ_L during the time interval Δt. Hence, $\overline{D} = (\langle\Delta\Theta_L\rangle_{\rm rms})^2$. We consider one wave packet along the field line, so during a bounce period the particle's pitch angle changes only once, as it passes through the wave packet parallel to the wave.

The numerical precipitation flux is evaluated as:

$$S_{\rm pr}^{\rm num} = \frac{N\delta N_{\rm p}}{\Delta t}. \tag{A12}$$

Here $\delta N_{\rm p} = N_{\rm p\,lost}/N_{\rm p}$ is the relative number of particles, precipitated during time interval Δt.

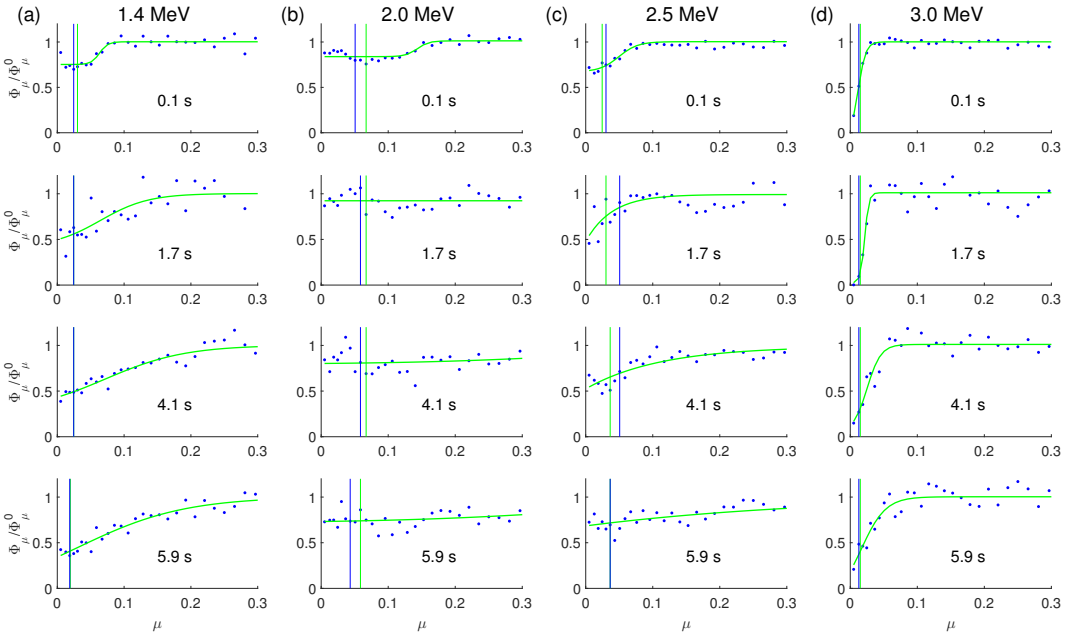

Figure A1. Distribution function, obtained in simulation (blue dots), and approximation (A14) (green lines). Vertical lines correspond to the points μ_*, calculated for $\langle\Delta\mu\rangle^{\rm lin}_{\rm rms}$ (green) and $\langle\Delta\mu\rangle^{\rm num}_{\rm rms}$ (blue).

The particle flux through the loss cone boundary caused by the quasi-linear diffusion can be estimated by integrating (A10) and taking into account the absence of particle sources and sinks at $\mu = 0$ and $\mu = 1$:

$$S^{\rm lin}_{\rm pr} = \frac{v_0}{2}\overline{D}\left.\frac{\partial\Phi}{\partial\mu}\right|_{\mu=\mu_{\rm c}} = \frac{v_0}{2}\frac{(\langle\Delta\mu\rangle_{\rm rms})^2}{4\mu_{\rm c}}\left.\frac{\partial\Phi_\mu}{\partial\mu}\right|_{\mu=\mu_{\rm c}}. \tag{A13}$$

Here $\langle\Delta\mu\rangle_{\rm rms} \approx \sqrt{4\mu(1-\mu)}\langle\Delta\Theta_L\rangle_{\rm rms}$ is root mean square deviation of μ after one resonant interaction in the vicinity of the loss cone $\mu = \mu_{\rm c}$, $\sqrt{1-\mu_{\rm c}} \approx 1$. The derivative $\partial\Phi_\mu/\partial\mu|_{\mu=\mu_{\rm c}}$ can be estimated using distribution function Φ_μ, obtained in the simulation. Analyzing the simulation results, particles with all phase values are summed up, which corresponds to phase averaging.

To obtain distribution function derivative $\partial\Phi_\mu/\partial\mu$, which can be used in (A13), we use a smooth approximation of the numerical distribution function. For the Gaussian wave packet, we choose the following approximation

$$\Phi^{\rm sm}_\mu = \Phi_1 + \Phi_2\tanh[\Phi_3(\mu - \mu^{\rm sm})]. \tag{A14}$$

Coefficients Φ_1, Φ_2, Φ_3 and $\mu^{\rm sm}$ are found by nonlinear least squares method under the conditions $\Phi_2 > 0$ and $\Phi_3 > 0$. Approximation (A14) is shown in Figure A1.

Root mean square deviation $\langle\Delta\mu\rangle_{\rm rms}$ can be calculated in two ways. One approach corresponds to analytical estimate by the stationary phase method $\langle\Delta\mu\rangle^{\rm lin}_{\rm rms}$ (10), and the other approach is based on using the numerical results:

$$\langle\Delta\mu\rangle^{\rm num}_{\rm rms} = \sqrt{\langle(\Delta\mu^{\rm num} - \langle\Delta\mu\rangle^{\rm num})^2\rangle}. \tag{A15}$$

Root mean square deviations, calculated as a function of μ, are shown in Figure A2. For calculating $\langle\Delta\mu\rangle^{\rm num}_{\rm rms}$ (A15), μ is divided in intervals equivalent to step 1° in Θ_L. For every energy W_0 and time moment T_i we find the point μ^*, for which $\langle\Delta\mu\rangle_{\rm rms}(\mu^*) \approx 2(\mu^* -$

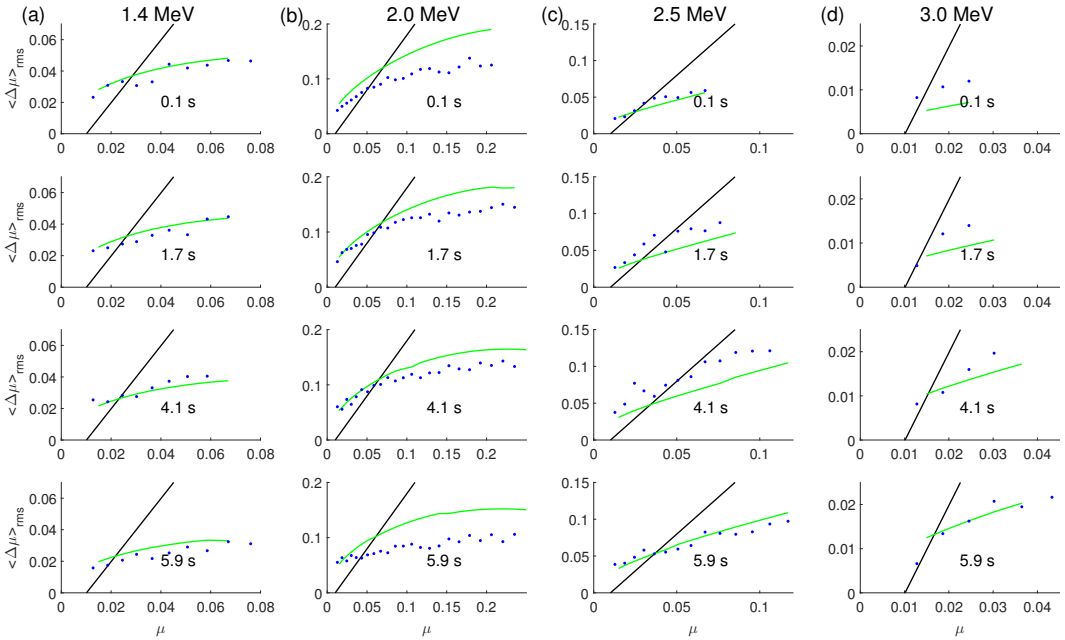

Figure A2. Root mean square deviations $\langle\Delta\mu\rangle_{\rm rms}^{\rm lin}$ (green lines) and $\langle\Delta\mu\rangle_{\rm rms}^{\rm num}$ (blue dots). Black lines correspond to $2(\mu-\mu_{\rm c})$.

$\mu_{\rm c}$) (in Figure A1, these points are shown by vertical lines). To calculate the quasi-linear precipitation flux (A13), we use the diffusion coefficient corresponding to $\langle\Delta\mu\rangle_{\rm rms}(\mu^*)$ and evaluate $\partial\Phi_\mu/\partial\mu$ at μ^* by using (A14).

Acknowledgments

The study conducted in this paper is theoretical and no data was used. This work was supported by the Russian Science Foundation, grant 15–12–20005.

References

Albert, J. M. (1993). Cyclotron resonance in an inhomogeneous magnetic field. *Physics of Fluids B*, *5*(8), 2744–2750. doi: 10.1063/1.860715

Albert, J. M. (2000). Gyroresonant interactions of radiation belt particles with a monochromatic electromagnetic wave. *J. Geophys. Res. Space Physics*, *105*(A9), 21191–21209. doi: 10.1029/2000JA000008

Albert, J. M., & Bortnik, J. (2009). Nonlinear interaction of radiation belt electrons with electromagnetic ion cyclotron waves. *Geophys. Res. Lett.*, *36*(12), L12110. doi: 10.1029/2009GL038904

Anderson, B. J., & Hamilton, D. C. (1993). Electromagnetic ion cyclotron waves stimulated by modest magnetospheric compressions. *J. Geophys. Res. Space Physics*, *98*(A7), 11369–11382. doi: 10.1029/93JA00605

Artemyev, A., Neishtadt, A. I., Vainchtein, D., Vasiliev, A. A., Vasko, I., & Zelenyi, L. (2018). Trapping (capture) into resonance and scattering on resonance: Summary of results for space plasma systems. *Communications in Nonlinear Science and Numerical Simulation*, *65*, 111–160. doi: 10.1016/j.cnsns.2018.05.004

Artemyev, A. V., Mourenas, D., Agapitov, O. V., Vainchtein, D. L., Mozer, F. S., & Krasnoselskikh, V. (2015). Stability of relativistic electron trapping by strong

whistler or electromagnetic ion cyclotron waves. *Physics of Plasmas*, *22*(8), 082901. doi: 10.1063/1.4927774

Artemyev, A. V., Neishtadt, A. I., Vasiliev, A. A., & Mourenas, D. (2017). Probabilistic approach to nonlinear wave-particle resonant interaction. *Phys. Rev. E*, *95*(2), 023204. doi: 10.1103/PhysRevE.95.023204

Belyaev, P. P., Kotik, D. S., Mityakov, S. N., Polyakov, S. V., Rapoport, V. O., & Trakhtengerts, V. Y. (1987). Generation of electromagnetic signals at combination frequencies in the ionosphere. *Radiophysics and Quantum Electronics*, *30*(2), 189–206. doi: 10.1007/BF01034491

Belyayev, P. P., Polyakov, S. V., Rapoport, V. O., & Trakhtengerts, V. Y. (1984). Fine structure of Alfven maser radiation. *USSR Report Earth Sciences JPRS UES*, *24*(2), 138.

Bespalov, P. A., & Trakhtengerts, V. Y. (1986). The cyclotron instability in the Earth radiation belts. In M. A. Leontovich (Ed.), *Reviews of plasma physics* (Vol. 10, pp. 155–293). Plenum Publ., N.Y.

Demekhov, A. G. (2007). Recent progress in understanding Pc1 pearl formation. *J. Atmos. Sol. Terr. Phys.*, *69*(14), 1609–1622. doi: 10.1016/j.jastp.2007.01.014

Demekhov, A. G., Trakhtengerts, V. Y., Rycroft, M. J., & Nunn, D. (2006). Electron acceleration in the magnetosphere by whistler-mode waves of varying frequency. *Geomagnetism and Aeronomy*, *46*(6), 711–716. doi: 10.1134/S0016793206060053

Engebretson, M. J., Keiling, A., Fornacon, K.-H., Cattell, C. A., Johnson, J. R., Posch, J. L., ... Rème, H. (2007). Cluster observations of Pc 1 2 waves and associated ion distributions during the October and November 2003 magnetic storms. *Planetary and Space Science*, *55*(6), 829–848. doi: 10.1016/j.pss.2006.03.015

Engebretson, M. J., Posch, J. L., Westerman, A. M., Otto, N. J., Slavin, J. A., Le, G., ... Lessard, M. R. (2008). Temporal and spatial characteristics of pc1 waves observed by st5. *J. Geophys. Res. Space Physics*, *113*(A7), A07206. doi: 10.1029/2008JA013145

Engebretson, M. J., Posch, J. L., Wygant, J. R., Kletzing, C. A., Lessard, M. R., Huang, C.-L., ... Shiokawa, K. (2015). Van Allen probes, NOAA, GOES, and ground observations of an intense EMIC wave event extending over 12 h in magnetic local time. *J. Geophys. Res. Space Physics*, *120*(7), 5465–5488. doi: 10.1002/2015JA021227

Fraser, B. J., & Nguyen, T. S. (2001). Is the plasmapause a preferred source region of electromagnetic ion cyclotron waves in the magnetosphere? *J. Atmos. Sol. Terr. Phys.*, *63*(11), 1225–1247. doi: 10.1016/S1364-6826(00)00225-X

Grach, V. S., & Demekhov, A. G. (2018a). Resonance interaction of relativistic electrons with ion-cyclotron waves. i. specific features of the nonlinear interaction regimes. *Radiophysics and Quantum Electronics*, *60*(12), 942–959. doi: 10.1007/s11141-018-9860-0

Grach, V. S., & Demekhov, A. G. (2018b). Resonant interaction of relativistic electrons with electromagnetic ion–cyclotron waves. ii. integral parameters of interaction regimes. *Radiophysics and Quantum Electronics*, *61*(6), 389–401. doi: 10.1007/s11141-018-9900-9

Jordanova, V. K., Albert, J., & Miyoshi, Y. (2008). Relativistic electron precipitation by emic waves from self-consistent global simulations. *J. Geophys. Res. Space Physics*, *113*(A3), A00A10. doi: 10.1029/2008JA013239

Kangas, J., Guglielmi, A., & Pokhotelov, O. (1998). Morphology and physics of short-period magnetic pulsations. *Space Science Reviews*, *83*, 435–512.

Karpman, V. I., Istomin, Y. N., & Shklyar, D. R. (1974). Nonlinear theory of a quasimonochromatic whistler mode packet in inhomogeneous plasma. *Plasma Phys.*, *16*(8), 685–703.

Keika, K., Takahashi, K., Ukhorskiy, A. Y., & Miyoshi, Y. (2013). Global char-

acteristics of electromagnetic ion cyclotron waves: Occurrence rate and its storm dependence. *J. Geophys. Res. Space Physics*, *118*(7), 4135–4150. doi: 10.1002/jgra.50385

Kennel, C. F., & Petschek, H. E. (1966). Limit on Stably Trapped Particle Fluxes. *J. Geophys. Res.*, *71*(1), 1–28. doi: 10.1029/JZ071i001p00001

Kubota, Y., & Omura, Y. (2017). Rapid precipitation of radiation belt electrons induced by emic rising tone emissions localized in longitude inside and outside the plasmapause. *J. Geophys. Res. Space Physics*, *122*(1), 293–309. doi: 10.1002/2016JA023267

Loto'Aniu, T. M., Fraser, B. J., & Waters, C. L. (2005). Propagation of electromagnetic ion cyclotron wave energy in the magnetosphere. *J. Geophys. Res. Space Physics*, *110*(A7), A07214. doi: 10.1029/2004JA010816

Lundin, B. V., & Shkliar, D. R. (1977). Interaction of electrons with low transverse velocities with VLF waves in an inhomogeneous plasma. *Geomagnetism and Aeronomy*, *17*(2), 246–251.

Millan, R. M., & Thorne, R. (2007). Review of radiation belt relativistic electron losses. *J. Atmos. Sol. Terr. Phys.*, *69*(3), 362–377. doi: 10.1016/j.jastp.2006.06.019

Morley, S. K., Friedel, R. H. W., Cayton, T. E., & Noveroske, E. (2010). A rapid, global and prolonged electron radiation belt dropout observed with the global positioning system constellation. *Geophys. Res. Lett.*, *37*(6), L06102. doi: 10.1029/2010GL042772

Mursula, K. (2007). Satellite observations of Pc 1 pearl waves: The changing paradigm. *J. Atmos. Sol. Terr. Phys.*, *69*(14), 1623–1634. doi: 10.1016/j.jastp.2007.02.013

Omura, Y., Pickett, J., Grison, B., Santolik, O., Dandouras, I., Engebretson, M., ... Masson, A. (2010). Theory and observation of electromagnetic ion cyclotron triggered emissions in the magnetosphere. *J. Geophys. Res. Space Physics*, *115*(A7), A07234. doi: 10.1029/2010JA015300

Omura, Y., & Zhao, Q. (2012). Nonlinear pitch angle scattering of relativistic electrons by emic waves in the inner magnetosphere. *J. Geophys. Res. Space Physics*, *117*(A8), A08227. doi: 10.1029/2012JA017943

Omura, Y., & Zhao, Q. (2013). Relativistic electron microbursts due to nonlinear pitch angle scattering by emic triggered emissions. *J. Geophys. Res. Space Physics*, *118*(8), 5008–5020. doi: 10.1002/jgra.50477

Pickett, J. S., Grison, B., Omura, Y., Engebretson, M. J., Dandouras, I., Masson, A., ... Constantinescu, D. (2010). Cluster observations of EMIC triggered emissions in association with Pc1 waves near Earth's plasmapause. *Geophys. Res. Lett.*, *37*(9), L09104. doi: 10.1029/2010GL042648

Santolik, O., Gurnett, D., Pickett, J., Parrot, M., & Cornilleau-Wehrlin, N. (2003). Spatio-temporal structure of storm-time chorus. *J. Geophys. Res. Space Physics*, *108*(A7), 1278. doi: 10.1029/2002JA009791

Shoji, M., Omura, Y., Grison, B., Pickett, J., Dandouras, I., & Engebretson, M. (2011). Electromagnetic ion cyclotron waves in the helium branch induced by multiple electromagnetic ion cyclotron triggered emissions. *Geophys. Res. Lett.*, *38*(17), L17102. doi: 10.1029/2011GL048427

Shprits, Y. Y., Chen, L., & Thorne, R. M. (2009). Simulations of pitch angle scattering of relativistic electrons with mlt-dependent diffusion coefficients. *J. Geophys. Res. Space Physics*, *114*(A3), A03219. doi: 10.1029/2008JA013695

Summers, D., & Thorne, R. M. (2003). Relativistic electron pitch-angle scattering by electromagnetic ion cyclotron waves during geomagnetic storms. *J. Geophys. Res. Space Physics*, *108*(A4), 1143. doi: 10.1029/2002JA009489

Thorne, R. M., & Kennel, C. F. (1971). Relativistic electron precipitation during magnetic storm main phase. *J. Geophys. Res.*, *76*(19), 4446–4453. doi: 10.1029/JA076i019p04446

Trakhtengerts, V., & Demekhov, A. (2007). Generation of Pc 1 pulsations in the regime of backward wave oscillator. *J. Atmos. Sol. Terr. Phys.*, *69*(14), 1651–1656. doi: 10.1016/j.jastp.2007.02.009

Trakhtengerts, V. Y. (1995). Magnetosphere cyclotron maser: Backward wave oscillator generation regime. *J. Geophys. Res.*, *100*(A9), 17205–17210. doi: 10.1029/95JA00843

Trakhtengerts, V. Y., & Rycroft, M. J. (2008). *Whistler and Alfvén mode cyclotron masers in space*. New York: Cambridge University Press.

Usanova, M. E., Mann, I. R., Bortnik, J., Shao, L., & Angelopoulos, V. (2012). Themis observations of electromagnetic ion cyclotron wave occurrence: Dependence on ae, symh, and solar wind dynamic pressure. *J. Geophys. Res. Space Physics*, *117*(A10), A10218. doi: 10.1029/2012JA018049